Shock Waves
DOI 10.1007/s00193-012-0388-5

ORIGINAL ARTICLE

An empirical model for the ignition of explosively dispersed aluminum particle clouds

K. Balakrishnan · A. L. Kuhl · J. B. Bell · V. E. Beckner

Received: 20 August 2011 / Revised: 20 April 2012 / Accepted: 25 May 2012
© Springer-Verlag 2012

Abstract An empirical model for the ignition of aluminum particle clouds is developed and applied to the study of particle ignition and combustion behavior resulting from explosive blast waves. This model incorporates both particle ignition time delay as well as cloud concentration effects on ignition. The total mass of aluminum that burns is found to depend on the model, with shorter ignition delay times resulting in increased burning of the cloud. After the Al particles ignite, a competition for oxidizer between the booster detonation products and Al ensues. A new mass-averaged ignition parameter is defined and is observed to serve as a useful parameter to compare cloud ignition behavior. Investigation of this variable reveals that both peak ignition as well as the time required to attain peak ignition, are sensitive to the model parameters. The peak degree of dissociation in the fireball is about 19 % and the associated energy can play a significant role on the dynamics of the problem. The peak degree of ionization is about 2.9 % and the energy associated with this is much lower than the other controlling factors. Overall, this study demonstrates that the new ignition model developed captures effects not included in other combustion models for the investigation of shock-induced ignition of aluminum particle clouds.

Keywords Blast wave · Turbulent mixing · Ignition · Dissociation · Ionization

Communicated by F. Zhang.

A condensed version of this manuscript was presented at the 23rd International Colloquium on the Dynamics of Explosions and Reactive Systems (ICDERS), Irvine, CA, July 24–29, 2011.

K. Balakrishnan (✉) · J. B. Bell · V. E. Beckner
Computational Research Division, Lawrence Berkeley National Laboratory, 1 Cyclotron Road, Berkeley, CA 94720, USA
e-mail: kaushikb@lbl.gov

A. L. Kuhl
Lawrence Livermore National Laboratory, 7000 East Avenue, Livermore, CA 94551, USA

1 Introduction

Aluminum is generally added to explosives due to its high energy content (∼7.4 kcal/g), which can release additional energy by afterburning during its explosive dispersal. However, the ensuing two-phase mixture involves the confluence and interplay of various physical phenomena that present several challenges to simulating the behavior. Aluminum, when encased in a shell surrounding a booster/driver explosive charge—termed as a shock dispersed fuel (SDF) charge [1]—has gained recent interest, with robust, adaptive numerical simulations being carried out by Kuhl et al. [2,3]. These studies investigated the turbulent mixing effects in the ensuing fireball, and matched experimental pressure traces and late time mean chamber pressures. Balakrishnan and Menon [4,5] have also carried out simulations using a different numerical strategy and have investigated the dispersion and burning characteristics of the particles behind explosions. The Al particles were shown to cluster due to their interaction with the fluid mechanic structures in the mixing layer, resulting in preferential ignition of the particles. Other research groups are also investigating afterburn effects in explosions [6,7].

Despite the above detailed studies, ignition mechanisms of Al need to be revisited, particularly for Al clouds driven by shock/blast waves. Most ignition models of Al particles in the literature are based only on the criterion of the particle heating up to a certain ignition temperature, after which it burns.

Published online: 28 June 2012

However, the applicability of such models for particle clouds is questionable since they may not capture all the combustion physics involved. For instance, shock tube experiments undertaken by Boiko et al. [8,9] show that Al particle ignition also depends on the mass loading of the cloud; this concentration dependence was first shown by Mason and Taylor [10], and later also reported by Cassel et al. [11,12]. Cassel [12] proposes a cooperative mechanism of Al combustion where burning is sporadically distributed in flamelets for low particle concentrations; at higher concentrations, however, burning was reported to be more-or-less uniformly distributed in the particle cloud. Such features can come into play in the combustion of Al clouds and must be accounted for, especially for highly energetic systems such as explosions and blast waves.

Al particle clouds can ignite and burn very different from individual particles. This is because in particle clouds, certain regions may ignite first, after which the flame can propagate to other hitherto unignited regions. Furthermore, competition for heat and/or oxidizer can also come into play when a cloud of Al particles is involved. Thus, it is essential to accurately model Al particle cloud ignition/combustion using robust three-dimensional simulations, rather than relying upon modeling a solitary particle in an isolated state of combustion. Available ignition delay data from experiments can be used to model the ignition event of Al particle clouds. To this end, a new Al ignition model that incorporates empirical data for ignition temperature, ignition delay time, and particle concentration, is developed in this study and the ignition characteristics of Al particle clouds behind explosions is investigated. Furthermore, using this model, the dynamics of vorticity in the ensuing fireball, the role of dissociation of air, and ionization of Al, are investigated in this study using robust, adaptive numerical simulations.

This paper is organized as follows: Sect. 2 presents the numerical formulation used in the present study; Sect. 3 summarizes the results, including the key discussions; the main conclusions drawn from this study are summarized in Sect. 4.

2 Numerical formulation

2.1 Governing equations

The two-phase gasdynamic conservation laws under dilute conditions as formulated by Nigmatulin [13] are considered for the current simulations. Here, both phases, viz., gas and solid, are governed by separate continuum laws, and they interact only through source terms that account for inter-phase mass, momentum and energy transfer. Furthermore, the model does not account for volume fraction effects, i.e., the dilute approximation; however, in the future, we will undertake two-phase explosions with dense particle effects also taken into account. We also neglect diffusion effects and assume the flow to be inviscid; however, viscosity and thermal conductivity come into play in the inter-phase interaction terms.

The governing equations and the inter-phase interaction terms are now summarized, and can also be found in Kuhl et al. [2,3] and Khasainov et al. [14]. For the gas-phase, the continuity, momentum, energy and species equations are detailed as:

$$\frac{\partial \rho}{\partial t} + \nabla \bullet (\rho \mathbf{u}) = \dot{\sigma}_s, \tag{1}$$

$$\frac{\partial \rho \mathbf{u}}{\partial t} + \nabla \bullet (\rho \mathbf{u}\mathbf{u} + p) = \dot{\sigma}_s \mathbf{v} - \dot{\mathbf{f}}_s, \tag{2}$$

$$\frac{\partial \rho E}{\partial t} + \nabla \bullet (\rho \mathbf{u} E + p\mathbf{u}) = -\dot{q}_s + \dot{\sigma}_s E_s - \dot{\mathbf{f}}_s \bullet \mathbf{v}, \tag{3}$$

$$\frac{\partial \rho Y_k}{\partial t} + \nabla \bullet (\rho \mathbf{u} Y_k) = \omega_k + \delta_k \cdot \dot{\sigma}_s \cdot \mu_c(\rho_s), \tag{4}$$

where ρ, $\mathbf{u}$ and p denote, respectively, the density, velocity and pressure of the gas; the bold variables represent vectors. In the energy equation, E represents the total energy, summarized as $E = e + 1/2\mathbf{u}\mathbf{u}$, where e is the specific internal energy of the gas. In the species equation, Y_k represents the mass fraction of the kth species, where $k = 1\ldots5$ corresponds to driver, air, aluminum, aluminum products or driver products; δ_k represents the Kronecker delta, which is 1 when $k =$ fuel, and 0 otherwise. The source term, ω_k, in the species equation, represents the mass production/comsumption per unit volume of the kth species, and is evaluated assuming a mixing-controlled, infinite chemistry reaction rate, since chemical kinetics data under the high pressures and temperatures encountered behind explosions is not available in literature. A two-step mixing is assumed, i.e., the gaseous aluminum is first allowed to react with air in stoichiometric proportions, followed by the reaction of the booster products with air. The term $\dot{\sigma}_s$ denotes the inter-phase mass transfer rate, and is obtained using an empirical function of the Reynolds number; this term is included only when $k =$ fuel; the term μ_c is an ignition probability function; both these terms will be defined later.

The thermodynamics is summarized in [2,15]. Piecewise quadratic curve-fit expressions for e as a function of the gas temperature, T, are obtained from the Le Chatelier diagram [2], and the quadratic coefficients are mass-averaged in cells where more than one species exists, with the additional assumption that the individual species are in thermodynamic equilibrium. The Jones–Wilkins–Lee (JWL) equation of state is used in the regions corresponding to the detonation product gases, and the perfect gas equation of state in "pure" air regions. More details on the thermodynamics can be found in [2,15], including also the curve-fit expressions for the different species.

Similar governing equations are solved for the particle phase and are summarized below for the continuity, momentum and energy equations:

$$\frac{\partial \sigma}{\partial t} + \nabla \bullet (\sigma \mathbf{v}) = -\dot{\sigma}_s, \tag{5}$$

$$\frac{\partial \sigma \mathbf{v}}{\partial t} + \nabla \bullet (\sigma \mathbf{v}\mathbf{v}) = -\dot{\sigma}_s \mathbf{v} + \dot{\mathbf{f}}_s, \tag{6}$$

$$\frac{\partial \sigma E_s}{\partial t} + \nabla \bullet (\sigma \mathbf{v} E_s) = \dot{q}_s - \dot{\sigma}_s E_s + \dot{\mathbf{f}}_s \bullet \mathbf{v}, \tag{7}$$

where σ and $\mathbf{v}$ denote, respectively, the density and velocity of the solid particle phase. In the energy equation, the term E_s denotes the thermal energy of the solid particles, and is obtained as $E_s = c_s T_s$, where c_s is the heat capacity of Al, and T_s is the particle temperature.

The terms on the right hand side of the above governing equations represent the inter-phase interaction terms that represent mass, momentum and energy transfer between the two phases. These terms are summarized [14]:

$$\dot{\mathbf{f}}_s = \frac{3}{4}\frac{\rho}{\rho_s}\frac{\sigma}{d_s} C_D (\mathbf{u} - \mathbf{v})\,|\mathbf{u} - \mathbf{v}|, \tag{8}$$

$$\dot{q}_s = \frac{6\sigma}{\rho_s d_s}\left[\frac{Nu \lambda_g (T - T_s)}{d_s} + \epsilon \sigma_{SB}\left(T^4 - T_s^4\right)\right], \tag{9}$$

where ρ_s and d_s denote, respectively, the particle material density and diameter; C_D is the drag coefficient, obtained as:

$$C_D = \frac{24}{Re_s} + \frac{4.4}{\sqrt{Re_s}} + 0.42, \tag{10}$$

where Re_s is the slip Reynolds number, given by $Re_s = \rho d_s |\mathbf{u} - \mathbf{v}|/\eta$, where η is the viscosity of the gas, obtained by a power law:

$$\frac{\eta}{\eta_0} = \left(\frac{T}{T_0}\right)^n. \tag{11}$$

Here, η_0 is the reference viscosity at a reference temperature, T_0, and n is a constant, typically < 1. In addition, λ_g is the thermal conductivity of the gas, ϵ is the emissivity, σ_{SB} is the Stefan–Boltzmann constant, and Nu is the Nusselt number, obtained as $Nu = 2 + 0.6 Pr \sqrt{Re_s}$. The Prandtl number, Pr, is set a constant value of 0.7, and is used to obtain λ_g using the formula $Pr = \eta C_p/\lambda_g$, where C_p is the specific heat of the gas at constant pressure. Since the problem involves reactive Al particles, an additional equation is solved for the particle number density, N_p [16]:

$$\frac{\partial N_p}{\partial t} + \nabla \bullet \left(N_p \mathbf{v}\right) = 0, \tag{12}$$

from which the instantaneous particle diameter, d_s, is obtained using the following formula [16]:

$$d_s = \left(\frac{6\sigma}{\pi N_p \rho_s}\right). \tag{13}$$

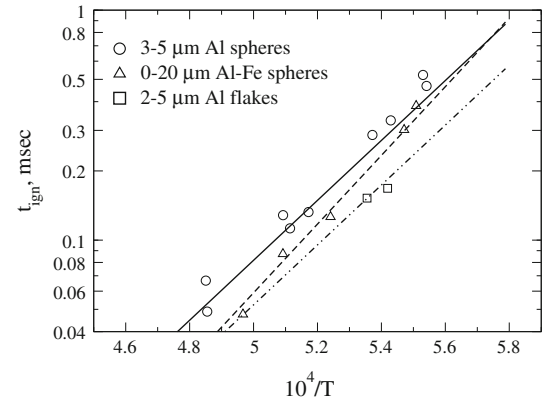

Fig. 1 Ignition time delays for Al spheres (*circles*), Al flakes (*squares*) and Al–Fe particles (*triangles*). The experimental data is from [8,9]

The term $\dot{\sigma}_s$, which represents the mass transfer rate, is turned on only when certain ignition criteria are attained. This study proposes an empirical ignition model to evaluate $\dot{\sigma}_s$, which is described below.

2.2 Ignition model

The new ignition model presented in this study for aluminum particle clouds is based on the works of Korobeinikov et al. [17] and Oran et al. [18], which were originally applied for detonation in gas-phase systems in lieu of an Arrhenius-type chemical kinetics. In this model, an induction parameter, $f(\mathbf{x}, t)$, is introduced, and is defined as follows:

$$\begin{aligned} &f(\mathbf{x}, t) = 0, \text{ initially;} \\ &0 \le f(\mathbf{x}, t) < 1, \text{ pre-ignition;} \\ &f(\mathbf{x}, t) \ge 1, \text{ post-ignition.} \end{aligned} \tag{14}$$

The evolution equation for $f(\mathbf{x}, t)$ is obtained by solving an additional equation, summarized as:

$$\frac{\partial \sigma f}{\partial t} + \mathbf{v} \bullet \nabla (\sigma f) = \frac{\sigma}{t_{ign}(T)} = \sigma A \exp\left(\frac{-E_a}{RT}\right), \tag{15}$$

where R is the universal gas constant and $t_{ign}(T_g)$ is the ignition time delay of the particles, which is empirically determined based on an Arrhenius-type model, with appropriate choices for the pre-exponential factor, A, and activation energy, E_a. Kuhl and Boiko [19] obtained an Arrhenius-type empirical curve-fit for t_{ign} based on the experimental data of Boiko et al. [8,9], with $A_{KB} = 6.25 \times 10^{10}$ for Al flakes and 4×10^{10} for Al spheres (for t_{ign} in seconds). These curve-fits and the original experimental data from [8,9] are presented in Fig. 1.

For both Al flakes as well as Al spheres, [19] obtained $E_{a,KB} = 60$ kcal/mol/K. This curve-fit, however, is only valid for $T \le 2{,}000$ K. For higher gas temperatures, we use

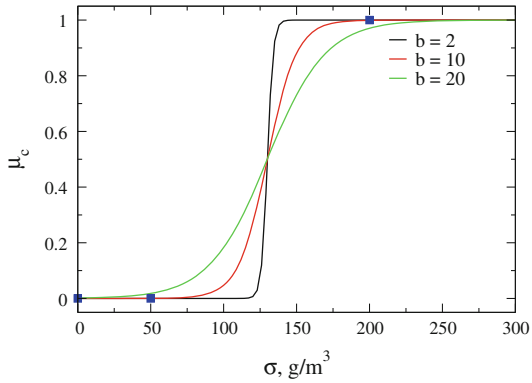

Fig. 2 Ignition probability function, μ_c. The *blue squares* represent experimental data from [8,9]

E_a = 22.8 kcal/mol/K from the data of Roberts et al. [20] for 20 μm Al spheres. Of particular interest in this study are 4–6 μm Al flakes, similar to the SDF experiments undertaken by Kuhl and Reichenbach [1]. Since A is not known for flakes when $T > 2{,}000$ K, we are free to experiment different values and determine their respective resulting late-time burning trends. Thus, the equation for t_{ign} is assumed to be of the form:

$$\frac{1}{t_{\text{ign}}(T)} = A_{\text{KB}} \exp\left(\frac{-E_{\text{a,KB}}}{RT}\right), \quad T \leq 2{,}000K; \tag{16a}$$

$$\frac{1}{t_{\text{ign}}(T)} = A/d_s^2 \exp\left(\frac{-E_a}{RT}\right), \quad T > 2{,}000K. \tag{16b}$$

With the use of this function for t_{ign}, the equation for $f(\mathbf{x}, t)$ can now be numerically solved in space and time. We specify one of the ignition criteria as $f(\mathbf{x}, t) > 1$. Essentially, $f(\mathbf{x}, t)$ is a measure of a time delay in the ignition of the Al particles.

Past studies have shown that aluminum particle cloud ignition is also determined by its concentration/loading [8–12]. For too small a particle loading, even though a few particles may ignite, they fail to ignite the cloud, as the particles are far apart and the energy release from the burning particles may not ignite other particles. Thus, a threshold particle loading is required for sustained burning of Al clouds, which has been measured to be 40 g/m^3 by [10], and ~150g/m^3 by Boiko et al. [8,9]. In the present study, a cloud ignition probability function, $\mu_c(\sigma)$, that varies between 0 and 1, is proposed [19] based on the data from [8,9], and is computed as

$$\mu_c(\sigma) = \frac{1}{1 + \exp\left[(\sigma^\circ - \sigma)/b\right]}, \tag{17}$$

where $\sigma^\circ = 130$ g/m^3 is a constant, obtained from Fig. 2. Different choices for b can lead to sharp or smooth changes in $\mu_c(\sigma)$ from 0 to 1, as observed in Fig. 2. We expect the transition from non-burning to burning in reality to be gradual, and so the value $b = 20$ is recommended. We note that in rapidly dispersing particle clouds, some regions in the flow-field may involve very dilute Al particle loading ratios, in which some burning particles may fail to ignite other hitherto unignited particles (see [8,9] for more discussions). Thus, we believe that cloud concentration effects need to be taken into account in empirical Al ignition/combustion models as well, unlike previous models. Our model is formulated and constructed to account for these effects.

The mass transfer rate, $\dot{\sigma}_s$, that occurs as a source term in the governing equations presented above, is multiplied by $\mu_c(\sigma)$ to account for cloud concentration effects (see Eq. 4). For $\dot{\sigma}_s$, we use the model of Khasainov et al. [14]:

$$\dot{\sigma}_s = 3\sigma\left(1 + 0.276\sqrt{Re_s}\right)/t_s, \tag{18}$$

where t_s an empirically determined burn time of the Al particles, obtained as $t_s = K d_s^2$, where $K = 150$ s/cm^2 [14]. This model assumes that the Al burning is primarily diffusive in nature, wherein the diffusion of oxidizer dictates the overall mass transfer rates. However, for small particles, as outlined by Vulis [21], it is possible that Al particle combustion can also be kinetically limited. Thus, hybrid Al burning laws have been recently proposed that account for both burning trends. One such model was proposed by Zhang et al. [22] and also used later by Briand et al. [16]; we plan to use this model for future investigations.

Often a cutoff particle temperature is used to model ignition of Al particles which, however, may not be valid for all particle sizes and/or oxidizer concentrations. Based on Al particle experiments, Gurevich et al. [23] obtained an empirical curve-fit for the ignition temperature (T_{ign}) as a function of oxidizer concentration (C_{ox}), particle size and gas thermal conductivity, summarized as:

$$T_{\text{ign}} = T_{\text{mp}} - 0.6\frac{C_{\text{ox}}^{0.3}}{\lambda_g} \cdot d_s \cdot \exp(-0.85\sqrt{(d_s)}), \tag{19}$$

where T_{mp} is the melting point of aluminum oxide, 2,300 K. This equation is employed to determine T_{ign} and the occurrence of Al ignition locally is defined when the following two conditions hold:

$$T_s(\mathbf{x}, t) > T_{\text{ign}}(C_{\text{ox}}, d_s, \lambda_g) \quad \text{and} \quad f(\mathbf{x}, t) \geq 1. \tag{20}$$

With these multiple ignition criteria in place, we have an empirical model that accounts for solid particle temperature, oxidizer concentration, Al cloud concentration effects, and the gas temperature, unlike previous empirical models that only accounted for some of these effects. Furthermore, the proposed Al ignition model is generic and can also be applied to other high-speed Al combustion problems, such as planar shock wave-Al cloud interactions, etc.

2.3 Numerical methods

The governing equations are integrated using high-resolution upwind methods that are higher-order generalizations of Godunov's method with efficient Riemann solvers detailed in [24–26]. The Riemann solver for the dilute multiphase mixture is based on Collins et al. [27]. In order to resolve the finer scales in the turbulent mixing layer, local adaptive mesh refinement (AMR) is used, based on [28]. The energy-bearing scales that are of preponderance are resolved using this AMR technique, and is consistent with the ILES approach [29]. In this approach, high-order finite-volume schemes capture the inviscid cascade of kinetic energy through the inertial range, and the inherent numerical dissipation of the scheme acts as an implicit subgrid model. One drawback, however, is that due to the absence of a physical viscosity, the dissipation of turbulent kinetic energy at the grid scale is not accurately characterized. Past studies reveal that provided a sufficiently fine grid is employed, most of the energy-bearing scales of relevance can be resolved and reasonable results can be obtained, even without accounting for the very small scales. More discussions can be found in the book by Grinstein et al. [29].

Typically, four levels of refinement are used at the beginning of the simulations, and as the blast wave and the fireball expand outwards, the number of AMR levels of refinement are progressively decreased. Recent studies [2,3] have shown this simulation strategy to be robust and efficient for the problem under investigation and is therefore employed in this study. Another efficient way to capture the fluid physics without the use of large number of degrees of freedom (DOF) is to employ the high order accurate spectral volume solver of Kannan [30,31], where it was shown that a relatively small number of DOF can capture most of the flow physics quite accurately. Other such numerical techniques can also be employed in the future and the efficacy of the results can be used to judge the robustness of the different solvers.

3 Results

3.1 Effect of ignition model

Simulations are carried out for an SDF charge that comprised 0.5 g of a spherical PETN booster charge surrounded by a cylindrical casing of 1 g of aluminum flakes with a thickness of 4–6 μm [2,3]. The charge is placed at the center of a cubic box of volume $25 \times 25 \times 25$ cm^3 (15.6 l), and free-slip boundary conditions are applied at the walls. Thus, we have ~3.8 g of oxygen for 0.5 g of booster and 1 g of Al, which is a globally fuel lean scenario. At early times, however, as the Al starts to burn, availability of oxygen is limited in the vicinity of the particle cloud, and late time turbulent mixing plays a crucial role in supplying the oxidizer from the outer regions of the box to the burning particles.

For the PETN booster, constant volume explosion pressure is initialized, including a 1 % perturbation to the density and energy; a similar approach has been used in many past studies undertaken by the authors [2,32]. The base grid is $80 \times 80 \times 80$, with four levels of refinement used at early times to resolve the finer turbulent scales, after which the number of levels are progressively reduced as the scales grow larger. This resolution for the finest level (fourth level), $\Delta_4 = 0.2$ mm, suffices for the current problem, as evidenced by comparisons to experiments presented in recent studies [2,3], albeit without the ignition model. Details on the dispersion of aluminum particles can be found in [4,5]. The goal here is to demonstrate the effect of the cloud ignition model on the late time dynamics of Al combustion and turbulent mixing in the fireball. Also of interest is to understand the vorticity dynamics in the mixing layer, the role of dissociation of air, and ionization of aluminum.

Adiabatic flame temperatures for Al-air combustion is ~4,300 K. As mentioned previously, due to the unavailability of ignition time delay experimental data for Al flakes at gas temperatures higher than 2,000 K, different values for A are considered in the range 10^8–10^9 (Eqn. 16b). For regions where $T < 2{,}000$ K, we use the Kuhl–Boiko curve-fit [19] to obtain t_{ign} (Eq. 16a). Moreover, we consider one additional simulation case where we extend the Kuhl–Boiko curve-fit for all gas temperature regimes. For illustration sake, when we refer to $A = 1 \times 10^8$, we obtain t_{ign} with the use of the Kuhl–Boiko curve-fit for $T < 2{,}000$ K, and $A = 1 \times 10^8$ for $T > 2{,}000$ K (Eq. 16).

For the different test cases, the respective gas temperature fields at 70 μs are presented in Fig. 3 (all the color images in this paper depict the $X-Y$ axis at the mid Z plane). The flow-field involves a leading blast wave, followed by a turbulent, two-phase fireball where the fuel and oxidizer mix and burn. The blast wave propagates outward and leads the fireball. The primary interest in this study is to understand the turbulent fireball. Rayleigh–Taylor instabilities are observed in the fireball, as also previously reported in explosion studies [3–5,32], due to the acceleration of a high-density gradient interface. Mushroom-like structures form at the tip of these Rayleigh–Taylor structures due to shear-driven Kelvin–Helmholtz instability.

For $A = 1 \times 10^8$, although some regions of the Al particle cloud ignite, they are quenched before the combustion energy release can ignite nearby regions; that is, the cloud does not sustain burning after ignition as the heat loss exceeds the combustion energy release. Mathematically speaking, the ignition time delays are too long to sustain burning and therefore the burning is limited. For $A = 2.5 \times 10^8$, more regions of the fireball involve Al burning; however, a few blue/green

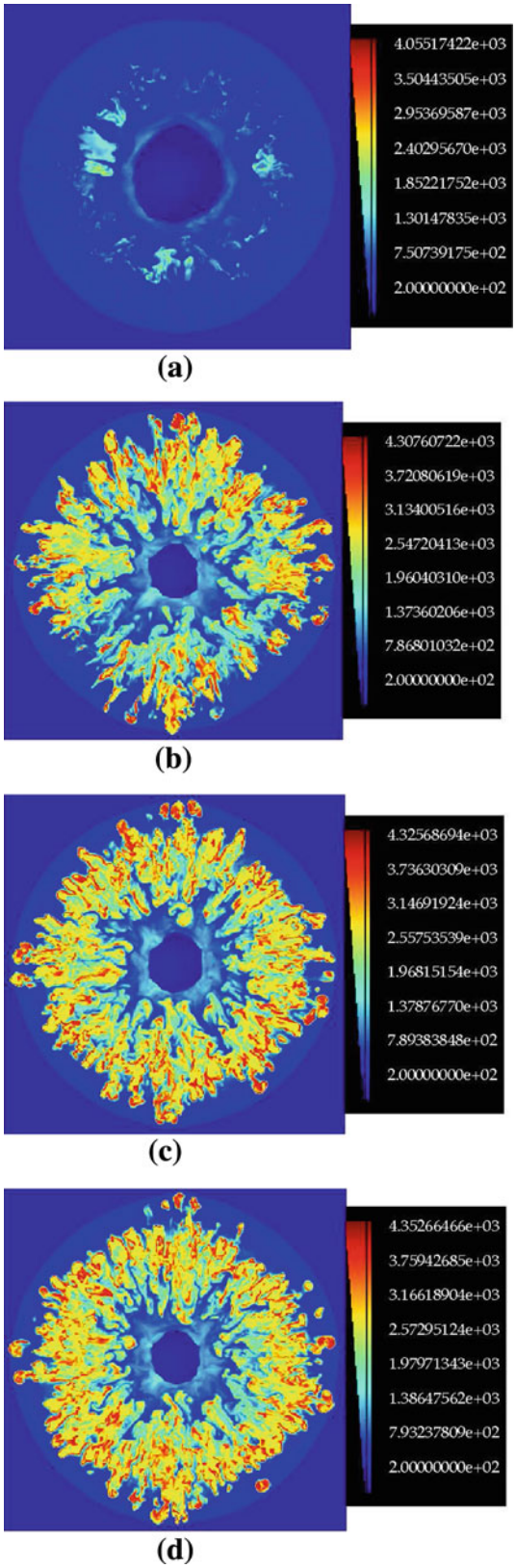

Fig. 3 Color scale visualization of a cross-section of the gas temperature field at 70 μs for different assumed values of A: **a** 1×10^8; **b** 2.5×10^8; **c** 1×10^9; **d** Kuhl–Boiko. The *scale* denotes the gas temperature in K

regions are evident in the mixing zone from Fig. 3b, indicating that in these regions the Al ignition time delay does not permit significant Al burning levels; in these blue/green regions, the chemical reaction between the booster and the ambient air is more dominant, and so the resulting flame temperatures in these regions conform to hydrocarbon burning-like temperatures, rather than Al combustion. With the use of the Kuhl–Boiko curve-fit, the ignition time delays are short, resulting in enhanced burning of Al as is evidenced by the red/yellow regions in Fig. 3d. However, observing Fig. 3c, d, we conclude that the Al burning trends for $A = 1 \times 10^9$ and with the Kuhl–Boiko curve-fit used at all temperature ranges, are nearly similar. These results qualitatively demonstrate that the ignition model does have a significant influence on the late-time Al burning characteristics, and consequently the fireball temperatures.

At late times, the leading blast wave reflects off the side walls and reshocks the mixing layer. In addition, the secondary shock (see [3–5,32] for more details) reshocks the mixing layer and the confluence of these two shocks results in Richtmyer–Meshkov instabilities, which further enhance the turbulent mixing due to baroclinic vorticity generation in the fireball.

3.2 Afterburn effects

To quantify the above observation, the mass of solid Al remaining ($m_{\mathrm{Al}}^{\mathrm{solid}}$) with time is shown in Fig. 4a for the different A values, including also two additional cases corresponding to (i) extending the Kuhl–Boiko [19] curve-fit beyond 2,000 K and (ii) $A \to \infty$, i.e., $t_{\mathrm{ign}} = 0$. For $A = 2.5 \times 10^8$, 90 % of the Al is consumed; for smaller values of A—which is equivalent to a larger ignition delay—the burning is considerably reduced at late times; as the particle cloud and the fireball expand, relatively less heat is available to sustain the burning and so the particles quench. For $A = 1 \times 10^8$, since burning is significantly delayed, the particles are allowed to disperse, and the surrounding gases have significantly expanded; consequently, less energy/temperature is available to self-sustain Al burning in the cloud. However, for $A = 2.5 \times 10^8$, Al ignition is only partially delayed and about half the Al by mass burns before being quenched. The result with the Kuhl–Boiko curve-fit at all temperature regimes predicts a burning trend similar to that with $A = 1 \times 10^9$, exemplifying that the induction time delay introduced by the ignition model has less, albeit non-negligible, role on the burning characteristics of the particles for $A > 5 \times 10^8$ and for the Kuhl–Boiko cases; for these cases, the Al burning is limited by the availability of oxidizer and the heat transfer rate from the gas to the particles. As expected, the Al burning trend for $t_{\mathrm{ign}} = 0$ predicts the highest burning rates, since the ignition time delay is zero. This study demonstrates that Al ignition delay times directly impact overall burning trends.

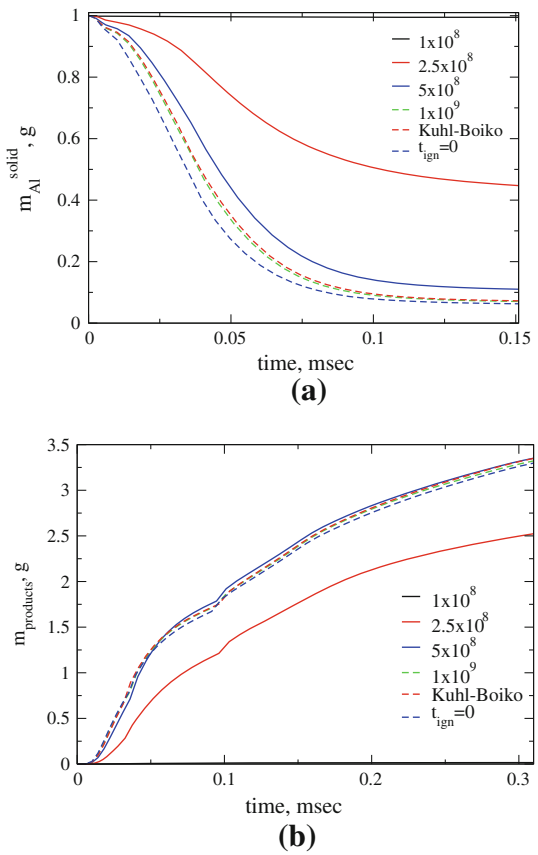

Fig. 4 Mass of **a** solid Al, **b** Al products remaining with time

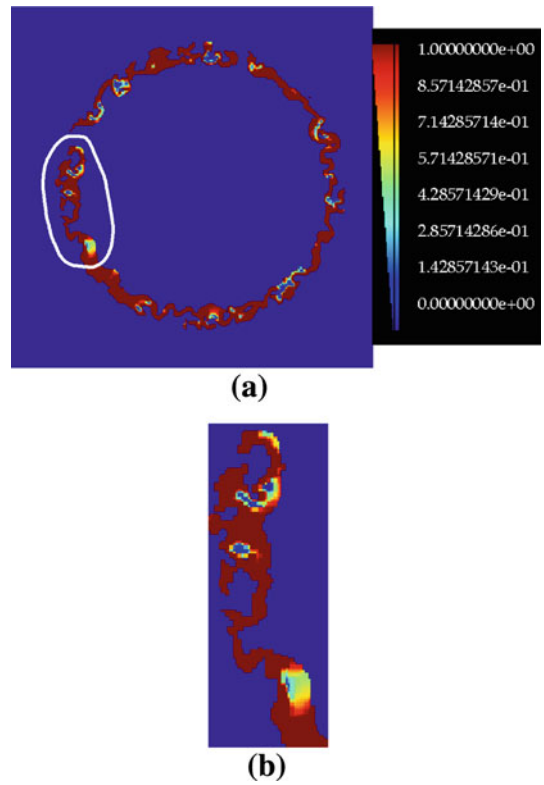

Fig. 5 Color scale visualization of the cross-section of the ignition variable f at 18 μs for the case with $A = 1 \times 10^9$. The *white circled region* from (**a**) is magnified and presented in (**b**), showing the corrugated ignition front

From Fig. 4a, the model predicts about 90 % of Al burns in the confined explosion, which is similar to past experimental results [1], albeit for a different chamber volume. These results also exemplify that the model predictions are in the expected burning trends.

Having demonstrated that aluminum combustion is directly related to the choice of A (in effect, on t_{ign}), the dependence of the mass of Al oxidation products (m_{products}) on the ignition model is presented in Fig. 4b. The trends suggest that less Al products are formed for $A = 1 \times 10^8$ and 2.5×10^8 as less Al evaporates. For $A = 5 \times 10^8$, even though slightly less Al products are formed by mass compared to the Kuhl–Boiko and $t_{\text{ign}} = 0$ cases, at later times, the re-shock effects change the mixing dynamics depending on the amount of Al that has ignited. This re-shock induced mixing can be observed in the form of a slight kink in Fig. 4b near 100 μs. It is also interesting to note that even though Al mass transfer nearly asymptotes around 100 μs from Fig. 4a, the Al products continue to be formed until times as long as 300 μs, as evident from Fig. 4b. This indicates that oxygen becomes limited at least around ~100 μs, after which the gaseous Al has to slowly mix with the outer air and only then burn into products. Thus, the availability of oxidizer at later times is limited, and turbulent mixing dictates the overall fuel burning trends at late times.

Since the induction parameter f used in this study depends on various parameters, it can vary spatially in a turbulent flow-field since heat sources, and fuel/oxidizer are all not available in plethora in all spatial regions at all times. Thus, it is of particular interest to understand the propagation of the ignition kernel, i.e., the propagation of the ignition front as the particles disperse outward. To this end, the contour of f is presented at 18 μs for the case with $A = 1 \times 10^9$ in Fig. 5a. The ignition front is observed to be clustered in shape around the Rayleigh–Taylor structures in the mixing layer, and the white circled region from Fig. 5a is magnified and presented in Fig. 5b, showing the corrugated/twisted ignition front. It has been recently shown in a different study that particles cluster as they disperse due to their interaction with the vortex rings in the mixing layer [5]. This inevitably results in the ignition front to also obtain a twisted shape, thereby increasing the overall surface area of the flame front. Regions with $f \sim 0.5$ are also observed, illustrating that not all regions of the particle cloud ignite to the same intensity. Analysis shows that there are ~32 fine cells across the ignition zone in Fig. 5; so the ignition zone is well resolved by the AMR technique.

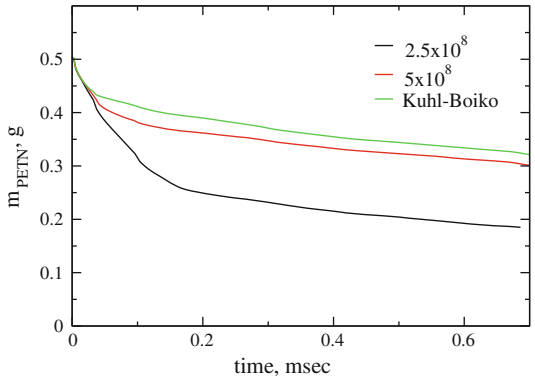

Fig. 6 Competition for oxidizer: mass of booster (m_{PETN}) remaining with time

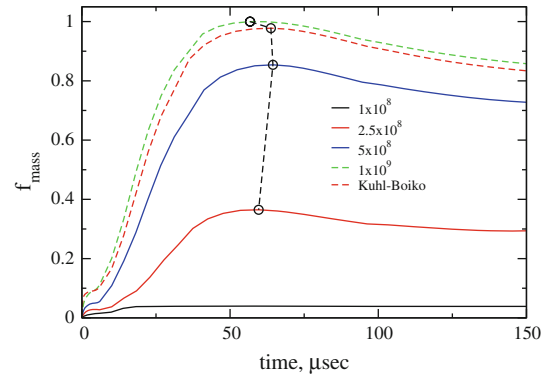

Fig. 7 Mass-averaged ignition variable f_{mass} for the different cases considered. The *black dashed line* joins the respective peaks, indicated by the *circles*

Since the problem under study involves two fuels, viz., PETN detonation products and Al, it is possible that both fuels can compete for the same oxidizer. To investigate this effect, we present in Fig. 6 the mass of the PETN detonation products, m_{PETN}, remaining with time for three of the cases: (1) $A = 2.5 \times 10^8$, (2) $A = 5 \times 10^8$ and (3) the Kuhl–Boiko curve-fit used for t_{ign} in all temperature regimes. Recall from before that among these three, Case (3) corresponds to the shortest Al ignition time delay and hence the highest Al burning levels. Case (1) corresponds to the longest ignition delay and so the least Al burning level, and Case (2) corresponds to an intermediate state between (1) and (3). It is apparent that when higher levels of Al burns, lesser PETN detonation products are consumed, and vice-versa. Furthermore, the three curves in Fig. 6 also overlap until about 0.03 ms, indicating that equal amounts of the booster are consumed for these three different cases at early times—when little or no Al is consumed. Beyond this time, however, the three curves diverge, with m_{PETN} following a trend exactly opposite to $m_{\mathrm{Al}}^{\mathrm{solid}}$. Thus, at early times (<0.03 ms) when little or no Al ignites, the booster detonation products have access to the necessary air supply to react. However, once Al ignites, a scenario emerges where the Al gas clouds the booster detonation products locally, and so the booster faces competition for oxidizer from the gaseous Al. This investigation reveals that the choice of the ignition model for Al, which dictates how much Al ignites/burns, can also indirectly affect the combustion of the booster detonation products due to the ensuing competition for oxidizer between the two fuels.

3.3 Mass-averaged induction parameter

It is often useful to quantify the overall global ignition trends in Al particle clouds. To this end, the above observations are quantified with the introduction of a new mass-averaged ignition variable, denoted as f_{mass}, which we define as:

$$f_{\mathrm{mass}} = \frac{\int \sigma f dV}{\int \sigma dV}, \tag{21}$$

where dV denotes a control volume. The variation of f_{mass} with time for the different cases considered in this study is presented in Fig. 7. f_{mass} rises from zero initially, albeit at different rates for the different cases depending on the choice of A. Around 50–60 μs, f_{mass} peaks, with the peaks ~1 for higher A. For $A \leq 5 \times 10^8$, f_{mass} never tends to unity, indicating that the entire Al cloud cannot burn in a self-sustained fashion and only partial burning occurs. This peak value of f_{mass} could also be used as a measure of particle cloud ignition, with lower peaks occurring for higher ignition delay times. The black dashed line joins the peaks, and shows that peak burning occurs earlier for the rapidly burning cases; however, the trend slightly shifts between $A = 5 \times 10^8$ and 2.5×10^8. Subsequently, as the particles disperse outward and enter relatively cooler regions, f_{mass} gradually decreases. This study illustrates that both peak ignition as well as the time taken to reach peak ignition, are dependent on the choice of the ignition model.

3.4 Vorticity dynamics in the mixing layer

Explosions are characterized by Rayleigh–Taylor and Richtmyer–Meshkov instabilities [2,4,5,32]. These instabilities involve density gradients misaligned with pressure gradients, which results in vorticity production due to baroclinic torque effects. This vorticity plays a key role in the turbulent mixing process and, consequently, on the afterburn; thus, it is of interest to understand the vorticity dynamics in the mixing layer. Contours of the vorticity field (in 1/s) at different times are presented in Fig. 8 for the case with the Kuhl–Boiko curve fit used for t_{ign}. At early times, vorticity is primarily concentrated at the tips of the Rayleigh–Taylor structures, whose alignment is biased in the radial direction. These mushroom-like structures consist of

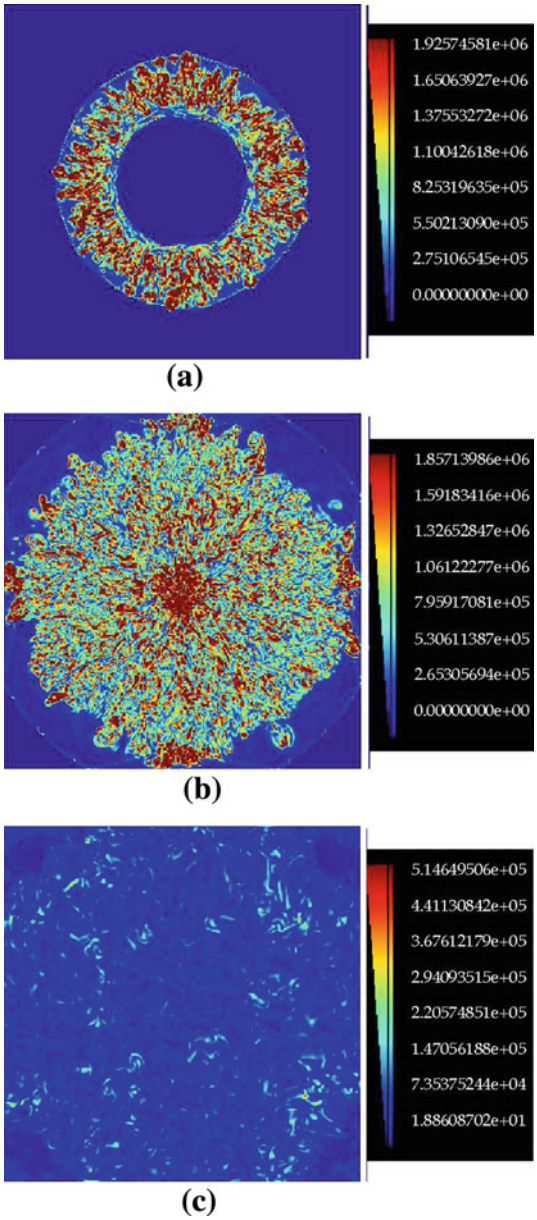

Fig. 8 Vorticity field at **a** 0.041 ms; **b** 0.096 ms; **c** 0.778 ms

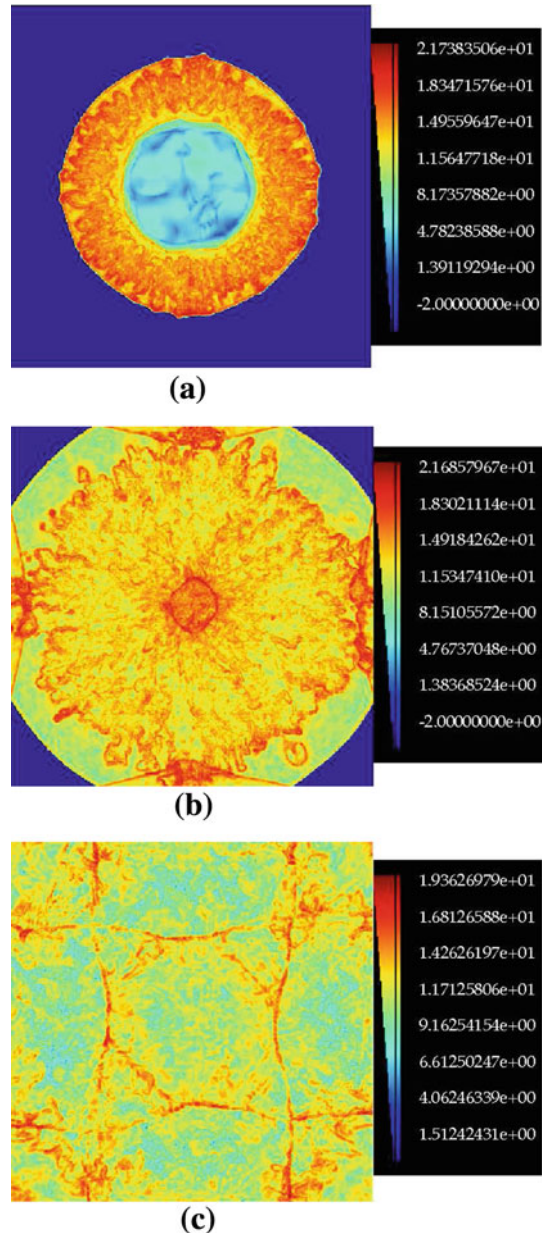

Fig. 9 Baroclinic torque field ($log(\exp(-2) + |\nabla p \times \nabla \rho|)$) at **a** 0.041 ms; **b** 0.096 ms; **c** 0.778 ms

coherent vortex rings at early times which, at later times, are broken down due to Kelvin–Helmoltz instabilities. Later, the coherence is lost (Fig. 8b), and vorticity is primarily concentrated in small filament-like structures, as also reported in recent high-fidelity Richtmyer–Meshkov simulations [33]. Finally, the vortex field exists as a bundle of vortex tubes, albeit at a reduced magnitude (Fig. 8c). While the peak vorticity magnitude at early time is $\sim 1.9 \times 10^6$/s, this transitions to $\sim 5 \times 10^5$/s at late times. At these late times, the vortex field is more-or-less isotropic and loses preferential alignment that is seen at the earlier times. This indicates that the late-time vortex structures—after multiple shock reflections and interactions—lose memory of the initial perturbation shapes.

Since vorticity is produced by the baroclinic mechanism, identifying the regions of high baroclinic torque in the mixing layer can provide insights on the production of vorticity in the mixing layer. To this end, Fig. 9 shows the baroclinic torque, more precisely $\log(\exp(-2) + |\nabla p \times \nabla \rho|)$, at different times for the same case. At early times (Fig. 9a), significant baroclinic effects persist at the tips of the Rayleigh–Taylor structures due to the high-density gradients. Thus, at these early times, density gradients identify the regions of significant baroclinic effects. Later, the regions of high baroclinic torque in Fig. 9b are concentrated in two regions: (1) near the center due to the secondary shock re-shocking the mixing layer,

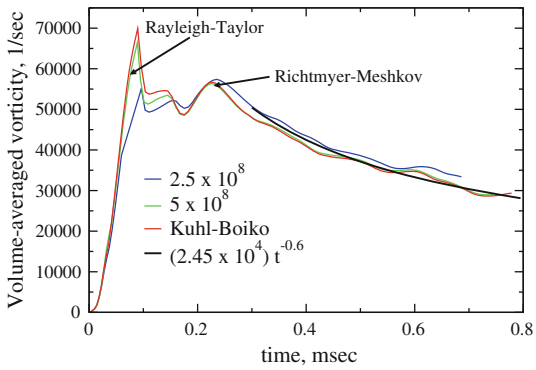

Fig. 10 Volume-averaged vorticity variation with time. The late-time vorticity decay conforms to $t^{-0.6}$, where t is in ms

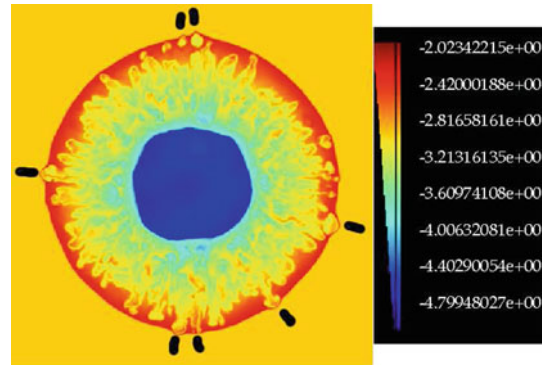

Fig. 11 The interaction of Rayleigh–Taylor structures with the primary blast wave. The *black markers* identify regions of particular interest

and (2) near the top, bottom, left and right, due to the primary shock reflecting from the end walls and interacting again with the mixing layer. At late times (Fig. 9c), baroclinic torque is primarily concentrated along pressure waves that propagate due to multiple reflections of the primary and secondary shock waves. Thus, at late times, pressure gradients identify the regions of prominent baroclinic effects. This investigation identifies qualitatively that vorticity production due to baroclinic effects are dictated initially by the strong density gradients, and later by the strong pressure gradients.

To quantify the observations in relation to the vorticity magnitudes in the fireball, we present in Fig. 10 the volume-averaged vorticity for three cases: (1) $A = 2.5 \times 10^8$, (2) $A = 5 \times 10^8$ and (3) Kuhl–Boiko curve-fit used for all T ranges. For Cases (2) and (3), since the ignition times are shorter, more Al burns, and therefore the average vorticity magnitude is higher than Case (1) during the early Rayleigh–Taylor instability growth phase. This is because higher heat release inevitably drives the initial fireball and due to the wider zone of mixing, higher average vorticity levels are encountered. Later, a second peak is observed for the total vorticity in the system near 0.25 ms due to the re-shocked Richtmyer–Meshkov instability. At late times, however, it is interesting to note that the total vorticity in the system is marginally higher for Case (1), particularly near 0.5–0.6 ms (the blue line in Fig. 10), since this case corresponds to less Al burning and therefore lower gas temperatures at late times; consequently, the average gas density is marginally higher for Case (1), and so is also the average vorticity. Subsequently, vorticity decays at later times at a rate conforming to $t^{-0.6}$, where t denotes the time in milliseconds. Future studies will have to determine the validity of this decay rate.

3.5 Rayleigh–Taylor structure interaction with blast wave

During early times, the Rayleigh–Taylor structures compete and merge, and grow into larger scales [4,5]. As the flow expands, these structures are driven radially outwards, after which they decelerate due to aerodynamic drag. If these structures grow to very large sizes, it is possible that they may decelerate less than the primary blast wave, in which case one or more structures can overtake the blast wave, contrary to classical Sedov-type explosions where the contact surface continuously lags behind the leading blast wave. Larger structures have lesser drag per unit mass than smaller structures [4,5] and can therefore travel greater distances. Such overtaking of the blast wave by the Rayleigh–Taylor structures was also reported recently for TNT explosions into Al particle clouds [4]. We present in Fig. 11 the quantity $log(\rho)$ at 0.052 ms for the case with the Kuhl–Boiko curve fit used for t_{ign}. The regions identified by the black markers in Fig. 11 clearly show such scenarios. Here, the deceleration of the Rayleigh–Taylor structures due to drag is less due to their relatively high densities, and so these structures penetrate the leading blast wave; in the vicinity of these penetrating structures, the local gas pressure is marginally higher than that behind the blast wave. Such anomalies have been reported in experiments too, see for instance Patterson et al. [34], where the authors report photographies of both luminous as well as non-luminous jets ejecting out of the leading blast wave. This has strong implications to experimental shock overpressure measurements, as also noted by [34]. This study confirms that such anomalies reported in past real-life explosions can also be captured in simulations.

3.6 Dissociation of air

Due to the high temperatures encountered in the explosive dispersal of Al particles (~4300 K), it is of interest to quantify the amount of dissociation of air in the fireball; in particular the peak dissociation magnitudes. To this end, we obtain empirical curve-fit expressions for the degree of dissociation, α_d, as a function of the gas temperature and density, using the tables presented by Gilmore [35] for air. These curve-fits are used to determine α_d at different times for the simulation corresponding to the Kuhl–Boiko curve fit, and the α_d contours are presented in Fig. 12. As evident, the

peak α_d is about 19 % at early times, and later about 17.5 %. More interestingly, at early times, the regions of high dissociation are primarily concentrated as small, unconnected, sporadic pockets. Subsequently, as the Al burning spreads to more regions, these pockets grow in size and soon attain large enough sizes where contiguous pockets start to interact, and then merge. Subsequently, as Al burning further spreads to even more regions, the pockets of dissociation get connected, resulting in a highly turbulent dissociation field that is continuous and stays linked, as shown in Fig. 12d.

We next determine whether the dissociation of air can play a prominent role on the gas dynamics of the problem, albeit using a crude technique. Using the dissociation energy of air, 8 kcal/g, and assuming 19 % peak α_d, results in a dissociation energy, $E_{diss.} = 0.19 \times 8 \sim 1.5$ kcal/g, which is commensurable with the energy release from the detonation of many high explosives (~1.1 kcal/g), the afterburn of carbon-rich high explosives (~3.6 kcal/g), and the Al combustion energy release (~7.4 kcal/g). Thus, we strongly believe that dissociation of air can indeed play a prominent role on the gas dynamics of the fireball.

3.7 Ionization of Al

Aluminum can also ionize at high temperatures and whether or not this can play a significant role for the problem under study is now ascertained. To this end, we employ the Saha equation to compute the electron concentration [36], summarized as:

$$\frac{N_e N_{Y+1}}{N_Y} = 2\frac{U_{Y+1}}{U_Y} \cdot C \cdot T^{3/2} \cdot \exp(-\chi_{Y,Y+1}/kT), \qquad (22)$$

where N_e is the concentration of electrons per unit volume, N_{Y+1} is the concentration of Al atoms in ionized state per unit volume (assumed = N_e), N_Y is the concentration of Al atoms per unit volume, the partition function ratio is obtained as $2 \cdot \frac{U_{Y+1}}{U_Y} = 2 \cdot \frac{1}{6} = \frac{1}{3}$, C is a constant and equals 2.414661×10^{15}, T is the local gas temperature in K, $\chi_{Y,Y+1}$ is the ionization energy for Al and equals 5.986 ev and k is the Boltzmann constant = 8.617343×10^{-5} ev/K. Inserting these relations in Eq. (22) results in the final form of the Saha equation as:

$$\frac{N_e^2}{N_{Al}} = 8.0489 \times 10^{14} \times T^{3/2} \times \exp(-5.986/kT). \qquad (23)$$

We denote the degree of ionization, α_i, as the ratio $\frac{N_e}{N_{Al}}$, and determine this quantity in space at different times, presented in Fig. 13. Similar to α_d, α_i, too, starts as discrete, sporadic pockets which later grow into larger sizes. Soon, contiguous pockets start to merge and at late times, take a shape that is chaotic but continuously connected along the outer edges of the fireball. Furthermore, the peak α_i is about 2.9 % at

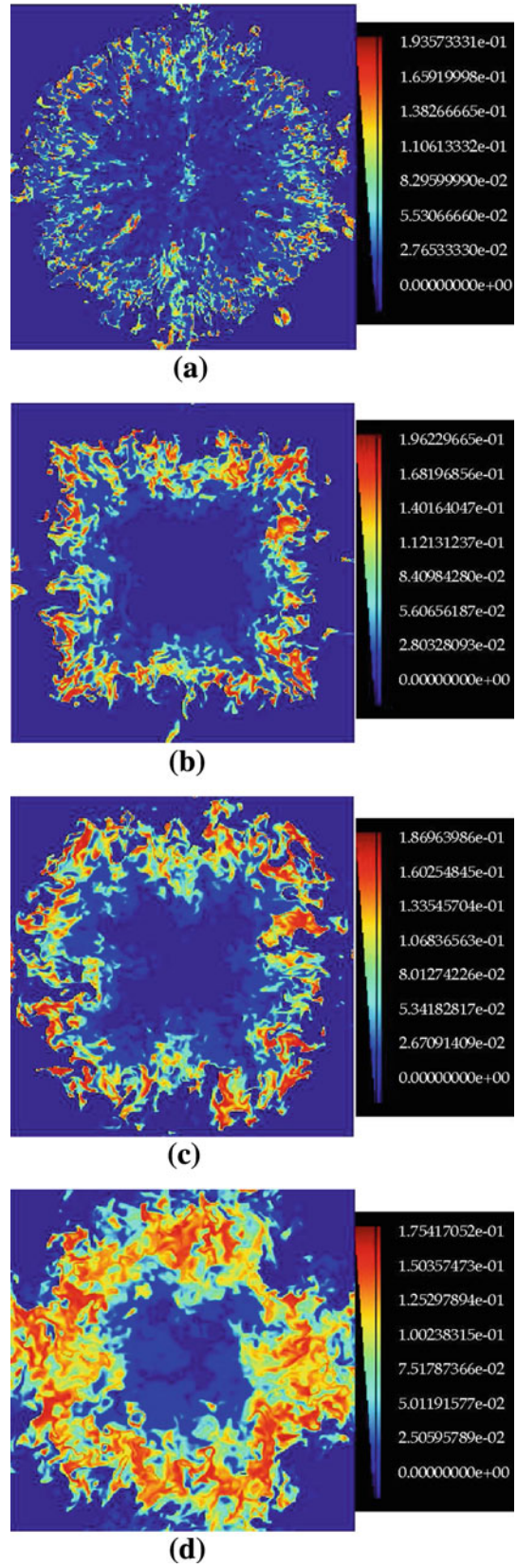

Fig. 12 Degree of dissociation at **a** 0.096 ms; **b** 0.168 ms; **c** 0.239 ms; **d** 0.778 ms

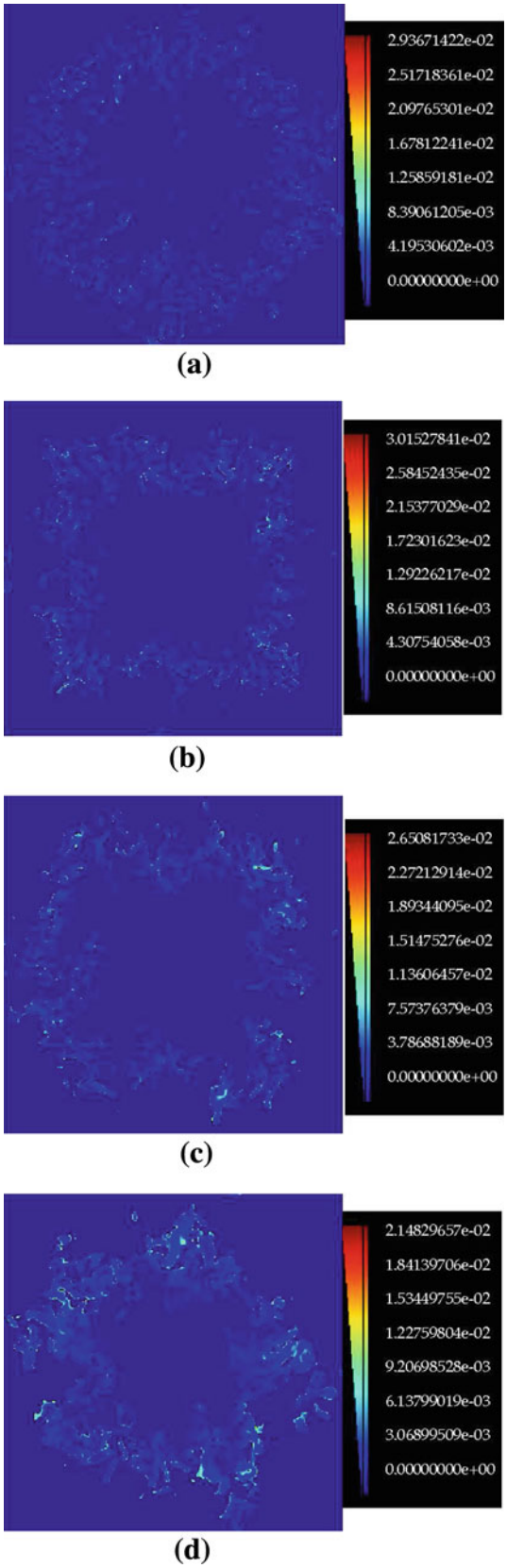

Fig. 13 Degree of ionization at **a** 0.096 ms; (b) 0.168 ms; (c) 0.239 ms; (d) 0.778 ms

early times and transitions to about 2.1 % at late times, as the late time temperatures slightly drop due to the entrainment of the outer cooler air into the fireball. In order to determine whether ionization of Al can play a prominent role on the gas dynamics, we multiply the observed peak α_i with the first ionization energy of Al (5.1 kcal/g) to obtain $E_{\text{ion.}} = 0.029 \times 5.1 \sim 0.15$ kcal/g, which is more than one order of magnitude smaller than the energies associated with Al combustion or the afterburn of the booster products. Thus, we envisage that ionization of Al could presumably have no role on the major gas dynamics of the problem.

4 Conclusions

A new empirical model is developed based on experimental data and applied to the investigation of ignition of aluminum particle clouds embedded in explosive blast waves. Effects not previously incorporated in some of the existing models are included in the current developments, and are coupled to the existing adaptive, two-phase numerical simulation strategy. With shorter ignition delay times used in the model, enhanced burning of the cloud occurs. The ignition kernel is distorted in shape due to the interaction of the particles with the vortex rings in the mixing layer. After the Al ignites, a competition for oxidizer between the booster detonation products and the gaseous Al ensues. A new mass-averaged ignition parameter is defined and its trends are compared for the different cases considered. Both peak ignition as well as the time required to attain peak ignition, are observed to depend on the model parameters. Both the degrees of dissociation and ionization initially appear as discrete, unconnected pockets; later, these pockets grow in size and contiguous pockets, then, start to interact and merge. Subsequently, these pockets become connected and appear as a chaotic but connected regions of dissociation and ionization. The peak degree of dissociation of air is about 19 % and it appears from an energy analysis that this can play a significant role on the gas dynamics of the fireball. The peak degree of ionization of Al is about 2.9 % and from similar energy considerations, appears to have almost no role on the dynamics of the problem. This study demonstrates that the ignition model developed here is useful to the study of aluminum particle cloud ignition and combustion behind explosions.

Acknowledgments This research work was performed under the auspices of the U.S. Department of Energy by the Lawrence Livermore National Laboratory under Contract DE-AC52-07NA27344, and supported by the Defense Threat Reduction Agency. The work at Lawrence Berkeley National Laboratory was performed under contract number DE-AC02-05CH11231. The simulations were performed at the ERDC High Performance Computing Center. The first author acknowledges interesting discussions held with Prof. David Frost of McGill University and Dr. Christer Fureby of the Swedish Defence Research Agency.

References

1. Kuhl, A.L., Reichenbach, H.: Combustion effects in confined explosions. Proc. Combust. Inst. **32**(2), 2291–2298 (2009)
2. Kuhl, A.L., Bell, J.B., Beckner, V.E.: Heterogeneous continuum model of aluminum particle combustion in explosions. Combust. Explos. Shock Waves **46**(4), 433–448 (2010)
3. Kuhl, A.L., Bell, J.B., Beckner, V.E.: Gasdynamic model of turbulent combustion in TNT explosions. In: 33rd International Combustion Symposium, Beijing, China, August 1–6 (2010)
4. Balakrishnan, K., Menon, S.: On the role of ambient reactive particles in the mixing and afterburn behind explosive blast waves. Combust. Sci. Tech. **182**(2), 186–214 (2010)
5. Balakrishnan, K., Menon, S.: On turbulent chemical explosions into dilute aluminum particle clouds. Combust. Theory Model. **14**(4), 583–617 (2010)
6. Zarei, Z., Frost, D.: Simplified modeling of blast waves from metalized heterogeneous explosives. Shock Waves **21**(5), 425–438 (2011)
7. Fedina, E., Fureby, C.: Investigating ground effects on mixing and afterburning during a TNT explosion. In: 23rd International Colloquium on the Dynamics of Explosions and Reactive Systems, Irvine, CA, July 24–29 (2011)
8. Boiko, V.M., Lotov, V.V., Papyrin, A.N.: Ignition of gas suspensions of metallic powders in reflected shock waves. Combust. Explos. Shock Waves **25**(2), 193–199 (1989)
9. Boiko, V.M., Poplavski, S.V.: Self-ignition and ignition of aluminum powders in shock waves. Shock Waves **11**(4), 289–295 (2002)
10. Mason, R.B., Taylor, C.S.: Explosion of aluminum powder dust clouds. Ind. Eng. Chem. **29**(6), 626–631 (1937)
11. Cassel, H.M., Das Gupta, A.K., Guruswamy, S.: Factors affecting flame propagation through dust clouds. Sympos. Combust. Flame Explos. Phenom. **3**(1), 185–190 (1949)
12. Cassel, H.M., Liebman, I.: The cooperative mechanism in the ignition of dust dispersions. Combust. Flame **3**, 467–475 (1959)
13. Nigmatulin, R.I.: Dynamics of Multiphase Media, Part I. Hemisphere, New York (1991)
14. Khasainov, B., Kuhl, A.L., Victorov, S., Neuwald, P.: Model of non-premixed combustion of Al-air mixtures. In: Proceedings of 14th APS Meeting on Shock Compression in Condensed Matter, vol. 845, issue 1, pp. 449–452 (2005)
15. Kuhl, A.L., Khasainov, B.: Quadratic model of thermodynamic states in SDF explosions. In: 38th International Conference of ICT Energetic Materials, Karlstruhe, Germany, June 26–29 (2007)
16. Briand, A., Veyssiere, B., Khasainov, B.A.: Modelling of detonation cellular structure in aluminum suspensions. Shock Waves **20**, 521–529 (2010)
17. Korobeinikov, V.P., Levin, V.A., Markov, V.V., Chernyi, G.G.: Propagation of blast waves in a combustible gas. Astronaut. Acta **17**, 529–537 (2010)
18. Oran, E.S., Boris, J.B., Young, T.R., Flanigan, M., Picone, M.: Simulation of gas phase detonations: introduction of an induction parameter model, NRL Memorandum Report 4255 (1980)
19. Kuhl, A.L., Boiko, V.M.: Ignition of aluminum particles and clouds. In: 41st International Conference of ICT Energetic Materials, Karlstruhe, Germany, June 29–July 2 (2010)
20. Roberts, T.A., Burton, R.L., Krier, H.: Ignition and combustion of aluminum/magnesium alloy particles in O_2 at high pressures. Combust. Flame **92**, 125–143 (1993)
21. Vulis, L.A.: Thermal Regimes of Combustion. McGraw-Hill, Maidenheach (1961)
22. Zhang, F., Gerrard, K.B., Ripley, R.C., Tanguay, V.: Unconfined aluminum particles-air detonation. In: Proceedings of the 26th ISSW, pp. 15–20, Gottingen, Germany (2007)
23. Gurevich, M.A., Lapkina, K.I., Ozerov, E.S.: Ignition limits of aluminum particles. Combust. Expl. Shock Waves **6**(2), 154–157 (1970)
24. Colella, P., Glaz, H.M.: Efficient solution algorithms for the Riemann problem for real gases. J. Comput. Phys. **59**, 264–289 (1985)
25. Bell, J.B., Colella, P., Trangenstein, J.A.: Higher order Godunov methods for general systems of hyperbolic conservation laws. J. Comput. Phys. **82**(2), 362–397 (1989)
26. Colella, P.: Multidimensional upwind methods for hyperbolic conservation laws. J. Comput. Phys. **87**, 171–200 (1990)
27. Collins, P., Ferguson, R.E., Chien, K.Y., Kuhl, A.L., Krispin, J., Glaz, H.M.: Simulation of shock-induced dusty gas flows using various models. AIAA Fluid Dynamics Conference, AIAA 94-2309 (1994)
28. Berger, M.J., Colella, P.: Local adaptive mesh refinement for shock hydrodynamics. J. Comput. Phys. **82**(1), 64–84 (1989)
29. Grinstein, F.F., Margolin, L.G., Rider, W.J. (eds.): Implicit Large-Eddy Simulation: Computing Turbulent Fluid Dynamics. Cambridge University Press, Cambridge (2007)
30. Liang, C., Kannan, R., Wang, Z.J.: A p-multigrid spectral difference method with explicit and implicit smoothers on unstructured triangular grids. Comput. Fluids **38**(2), 254–265 (2009)
31. Kannan, R., Wang, Z.J.: A study of viscous flux formulations for a p-multigrid spectral volume Navier-Stokes solver. J. Sci. Comput. **41**(2), 165–199 (2009)
32. Kuhl, A.L.: Spherical mixing layers in explosions. In: Bowen, J.R. (ed.) Dynamics of Exothermicity, pp. 291–320 + color plate 4 and 5. Gordon & Breach Publishers, The Netherlands (1996)
33. Thornber, B., Drikakis, D., Youngs, D.L., Williams, R.J.R.: The influence of initial conditions on turbulent mixing due to Richtmyer–Meshkov instability. J. Fluid. Mech. **654**, 99–139 (2010)
34. Patterson, A.M., Kingery, C.N., Rowe, R.D., Petes, J., Dewey, J.M.: Fireball and shock wave anomalies observed in chemical explosions. Combust. Flame **19**, 25–32 (1972)
35. Gilmore F.R.: Equilibrium Composition and Thermodynamic Properties of Air to 24, 000°K. U.S. Air Force Project Rand Research Memorandum, The Rand Corporation (1955)
36. Allen, C.W.: Astrophysical Quantities. pp. 33–37. University of London, Athlone Press, London (1973)